Applied Surface Science 537 (2021) 147896

Contents lists available at ScienceDirect

Applied Surface Science

journal homepage: www.elsevier.com/locate/apsusc

Galvanic oxidation of bimetallic Zn-Fe nanoparticles for oxygen scavenging

A. Castro[a], I. Carvalho[b], L. Marques[a], P.J. Ferreira[c,d,e], A. Cavaleiro[b], S. Carvalho[a,b], S. Calderon V.[a,b,*]

[a] CFUM-UP, Centre of Physics of University of Minho and Porto, Campus of Azurém, 4800-058 Guimarães, Portugal
[b] SEG-CEMMPRE Mechanical Engineering Department, University of Coimbra, 3030-788 Coimbra, Portugal
[c] INL – International Iberian Nanotechnology Laboratory, Av. Mestre José Veiga s/n, 4715-330 Braga, Portugal
[d] Materials Science and Engineering Program, The University of Texas at Austin, Austin, TX 78712, USA
[e] Mechanical Engineering Department and IDMEC, Instituto Superior Técnico, University of Lisbon, Av. Rovisco Pais, 1049-001 Lisboa, Portugal

ARTICLE INFO

Keywords:
galvanic potential, STEM
Moisture-activated
Relative humidity
Packaging

ABSTRACT

Bimetallic nanoparticles (NP) have demonstrated outstanding multifunctional characteristics, which depend on their size, distribution and composition. In this study, we show the possibility of tailoring the oxidation behavior of Zn-Fe bimetallic nanoparticles produced by magnetron sputtering and gas agglomeration system. Zn and Fe metals were coupled to promote faster oxidation of Zn, stimulating a galvanic mechanism due to the dissimilar corrosion potential in the nanoparticles. The results revealed Zn dissolution occurring at high humidity environments for bimetallic Zn-Fe nanoparticles where no intermix exists between Zn and Fe; however, such dissolution is excluded for ZnFe alloys. The effect of the galvanic couple on the Zn dissolution was confirmed by molecular dynamic simulations. This bimetallic system can be exploited as moisture-activated oxygen scavenger materials due to the acceleration in the oxidation mechanism.

1. Introduction

The production of bimetallic nanoparticles (NPs) with different structures and compositions have attracted a lot of attention due to their unusual characteristics, including catalysis, antibacterial, optical and magnetic properties [1,2]. These NPs are used in a large variety of technological applications such as textiles, biomedicine, food and agriculture, electronics, renewable energy and catalysis [3,4]. These applications are strongly influenced by the stability, size, distribution and composition of the nano-scaled systems, which can be tailored by the synthesis method.

Despite the known advantages of chemical methods in producing the bimetallic NPs, physical methods have gained significant interest due to their versatility and eco-friendly character. Magnetron sputtering is one of the most common vapor deposition techniques used by industry, which can be employed for the production of films, as well as NPs in very short deposition times. Previously, we have reported the production of carbon-supported Zn NPs, in which a detailed correlation between the production parameters and the control of size and distribution of the NPs is performed [5]. Such NPs exhibit an oxidation mechanism that can be controlled by the humidity in the environment, however, the maximum oxidation rate is limited. In this work, we propose a bimetallic system in which Fe accelerates the oxidation of Zn NPs by a galvanic couple, allowing us to better control the oxidation rate. In this context, fine control of NP size and composition is required. However, classic magnetron sputtering (MS) only offers a certain degree of control, which depends on the substrate chemistry, temperature, discharge power density, discharge pressure and complex kinetic processes.

As a new approach, several authors used a gas agglomeration technique that allows full control of the size and composition of the nanoparticles [6], demonstrating the successful production of NPs such as Fe [7], Au, Ag [8], Si [9], using a gas agglomeration system. Junlei Zhao, et al. [10], for instance, have demonstrated the possibility of controlling the shape and size of Fe clusters, by regulating the power applied to the target. The versatility of this technique also permits the production of multicomponent NPs, which offer not only the properties of each constituent but also acquire additional characteristics due to the catalytic process occurring between the elements, enhancing their functionality. These bimetallic NPs are usually divided into three types: core–shell NPs, dumbbell NPs and alloy NPs [11], where the distribution of the elements in the bimetallic NPs determines their function. A clear example of the gas agglomeration method to produce bimetallic NPs is the synthesis of bimetallic Fe-Au nanocubes for chemiresistive

* Corresponding author at: INL – International Iberian Nanotechnology Laboratory, Av. Mestre José Veiga s/n, 4715-330 Braga, Portugal.
E-mail address: secave44@gmail.com (S. Calderon V.).

https://doi.org/10.1016/j.apsusc.2020.147896
Received 22 May 2020; Received in revised form 8 September 2020; Accepted 11 September 2020
Available online 17 September 2020

gas sensors with good performance [7].

In this report, we proposed a combination of MS and gas agglomeration system to produce different Zn-Fe bimetallic NP arrangements. Diverse atomic ordering of Zn and Fe were used to demonstrate the possibility of activating a galvanic oxidation mechanism that can accelerate the oxidation of the NPs. Considering the moisture-activated oxidation properties of both Zn and Fe metals, the nanostructures were studied in high relative humidity environment (95–98% RH) to evaluate the evolution of the Zn-Fe NPs oxidation and determine the effect of Zn and Fe distributions on the oxidation kinetics of the NPs. The experimental results are supported by molecular dynamics simulation, demonstrating that the existence of an electric field created by the galvanic couple in a humid environment promoted the oxidation of the nanoparticles. To the authors' knowledge, a galvanic effect is for the first time demonstrated in these nanosystems, where Zn and Fe show dissimilar corrosion potentials and thus accelerate the oxidation of the NPs supported on carbon substrates. This shows the potential use of these NPs as oxygen scavenger for packaging applications.

2. Materials and methods

2.1. Materials production

Two production methods, illustrated in Fig. 1, were used to obtain a different distribution of the Zn and Fe elements. First, Zn and Zn-Fe nanostructures were deposited by classic magnetron sputtering onto TEM Cu-grids with an ultra-thin carbon layer (Fig. 1a), using a pulsed DC power supply. The power supply was plugged to a high purity Zn target (99.99%) or a Zn target modified with Fe pellets (99.95% purity). The substrates were located at 70 mm from a rotational substrate holder. The rotation speed of the substrate holder was maintained at 8 rpm to achieve homogeneous particle distribution. The temperature (313 K) and the substrate bias voltage (ground) remained constant during the depositions. The chamber was evacuated to 2×10^{-4} Pa and filled with Ar as an inert gas. The power density of the discharge for the Zn nanostructures was 0.2 W cm^{-2}, the discharge pressure 1.3 Pa and the deposition time 240 s. On the other hand, the power density for Zn-Fe nanostructures was modified (0.2 to 0.3 W cm^{-2}).

The second approach adopted was a hybrid process with both gas agglomeration system and magnetron sputtering (Fig. 1b). The system consists of a water-cooled cluster source, which exit slit (2 mm diameter) projects the clusters to the main chamber. This source was set with a Fe target (99.95% purity) of 50 mm in diameter and connected to a DC power supply. The nozzle is located at 95 mm from the substrate holder, which rotates continuously at 8 rpm. The main chamber is also equipped with a magnetron with a high purity Zn target (99.99%), located at 70 mm from the rotating substrate holder and provided with a DC power supply. The chamber and cluster source were evacuated to 3×10^{-3} Pa and 2×10^{-2} Pa, respectively, while the working pressure was adjusted to 7.2×10^{-1} Pa and 200 Pa, respectively. After optimizing the Fe power density (see supplementary information Fig S1), the cluster mean size obtained was 5.1 ± 1.6 nm. Those conditions were combined with the optimized conditions for the Zn nano-islands in the new system (0.35 Wcm^{-2}, 240 s). Thus, the Zn target was activated during 240 s a single time, while the Fe target was maintained ON for 2400 s. A full description of the deposition conditions can be seen in Table 1.

2.2. Methods

Morphological and structural characterization of the NPs was performed to study the effect of the deposition conditions on their crystallinity, size, and distribution. For this purpose, bright-field (BF) TEM images were acquired using a JEOL 2100 operated at 200 kV, equipped with the Gatan OneView camera. Particle segmentation was carried out to determine the size distribution and average size of the NPs using ImageJ [12]. The circularity of the particle was used to differentiate individual (circularity > 0.8) from coalesced NPs (circularity < 0.8).

To investigate the oxidation process of the NPs, the materials were subjected to a high (95–98%) relative humidity (RH) environment to monitor the NPs oxidation and determine its effect on the oxidation rate and oxidation mechanisms. An environment with 95–98% of RH was used to simulate the conditions in which the NPs are used as oxygen scavengers for food packaging applications. For high RH, the humidity was controlled using a saturated potassium sulfate solution prepared in distilled water. The solution was poured inside a desiccator and sealed until equilibrium was reached. Thereafter, the samples were inserted into the desiccator and sealed for 1 month.

HAADF STEM images were acquired on an aberration-corrected FEI Titan ChemiSTEM operated at 200 kV acceleration voltage. The extraction voltage was 3.35 kV and the pixel dwell time was set at 10 µs. A camera length of 135 mm was selected, which corresponds to acceptance angles ranging from 56 to 200 mrad, approximately.

Energy-dispersive X-ray spectroscopy mapping (EDX-mapping) was performed in an aberration-corrected FEI Titan ChemiSTEM equipped with a Super-X EDX detector. Iterative maps of 512 × 512 pixels were recorded with a dwell time per pixel of 10 µs at 200 kV to determine the elemental distribution. The maps were collected during 10 min of acquisition with a beam current of approximately 0.2nA measured on the phosphorus screen.

Particle segmentation was carried out to determine the size distribution and average size of the nanoparticles. At least 200 nanoparticles were used for determining the particle average size, following the methodology described by D.J. Groom et. al. [13].

2.3. Reax simulations

Molecular dynamics simulations were carried out using ReaxFF (reactive force field) [14], to study a ZnO (0001)/H_2O interface, using a parameterization to describe ZnO surfaces [15]. An electric field was

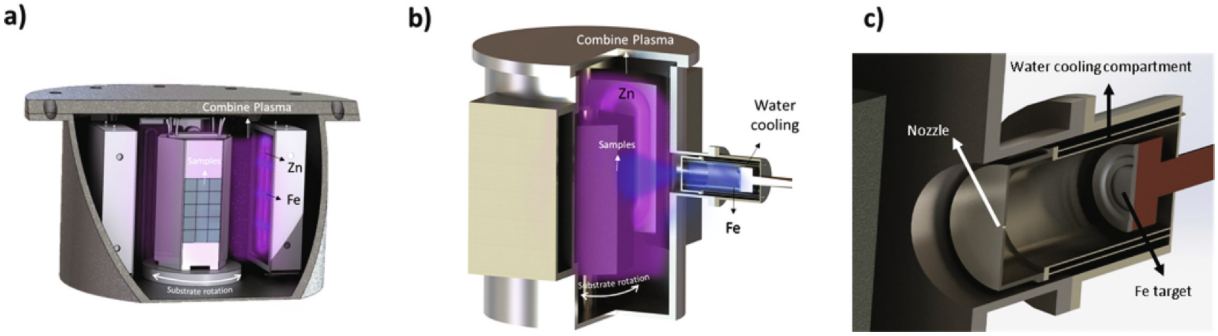

Fig. 1. Schematic representation of the systems used in this report a) classic magnetron sputtering chamber, b) magnetron sputtering chamber couple with an agglomeration gas system and c) a zoomed view of the gas agglomeration system in b).

Table 1
Deposition conditions for Zn and ZnFe nanoparticles by magnetron sputtering (first approach) and gas agglomeration system (second approach).

Sample	Zn Power Density [W cm^{-2}]	Fe Power Density [W cm^{-2}]	Working Pressure Main Chamber [Pa]	Working Pressure Cluster Source [Pa]	Deposition time of Zn [s]	Deposition time of Fe [s]
Classic Magnetron sputtering						
Zn	0.2	0	1.3	–	240	–
ZnFe	0.2–0.35	pellets	1.3	–	240	–
Gas agglomeration system						
Zn + Fe	0.35	5.1	0.72	200	240	2400

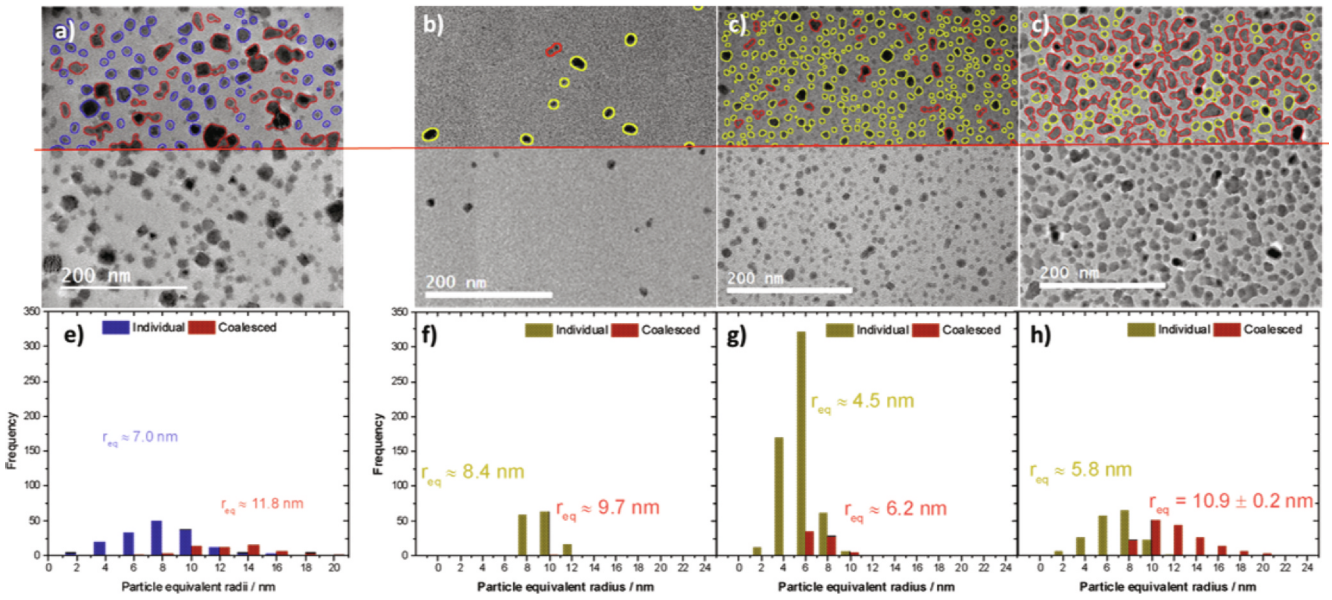

Fig. 2. BF-TEM images of Zn and ZnFe nanostructures deposited on carbon substrates at different discharge power density a) Zn at 0.2 W cm^{-2}, b) ZnFe at 0.2 W cm^{-2}, c) ZnFe at 0.3 W cm^{-2} and d) ZnFe at 0.35 W cm^{-2}, with their respective histograms for individual and coalesced particles size (e-h). The equivalent radius (r_{eq}) was calculated taking into consideration an equivalent circumference with the same area of each particle.

applied to understand the effect of the galvanic couple formed in the presence of Fe NP on the dissolution of Zn/ZnO.

ReaxFF uses a bond-order (BO) dependent potential, that allows the formation and breaking of bonds between atoms. The interaction energy is described by the Eq. (1):

$$E_{system} = E_{bond} + E_{over} + E_{under} + E_{lp} + E_{val} + E_{vdWaals} + E_{Coulomb} \quad (1)$$

The total energy on the system is divided into various partial energy terms that can be grouped into the bounded terms that include, bond energies (E_{bond}), penalty energies for over (E_{over}) and under coordination (E_{under}), lone pair energies (E_{lp}), valency angle energies (E_{val}), and the nonbonded terms, namely the van der Waals ($E_{vdWaals}$), and Coulomb ($E_{Coulomb}$) interaction energies. The bounded terms depend on the bond order (BO) parameter, which is determined dynamically based on the interatomic distances. The atomic charges are dynamically reassigned using geometry dependent charge equilibration methods [16,17] allowing for the description of charge transfer in chemical reactions.

The ZnO (0001)/H_2O interface model consisted of a slab of 11 layers of ZnO, with the (0001) surface saturated with oxygen atoms. The (0001) surface was solvated by a 20 Å layer of water, and a vacuum layer on the opposite surface. The size of the simulation box was 81.238 × 81.238 × 61 $Å^3$. The ZnO slab and water layer were preheated at a temperature of 300 K in two independent simulations before they were put in contact, and a 200 ps run was then performed. Simulations were done using the ReaxFF version as implemented on the LAMMPS software package [18,19]. Molecular dynamics runs were performed using the canonical ensemble (NVT) at a temperature of 300 K that was maintained using a Nosé-Hoover [20,21] thermostat with a damping constant of 1 fs. The atom trajectories were integrated using the velocity Verlet algorithm [22] with a time step of 0.1 fs. Periodic boundary conditions were applied on × and y directions and a reflective wall was used on the top and bottom boundaries of the z-direction to avoid the loss of atoms. An external electric field was applied on the z-direction, adding a force F = qE to each atom proportional the atomic charge. Different simulations were performed using different values for the electric field: 0.0 V/Å (no electric field), 0.10 V/Å, 0.20 V/Å, 0.32 V/Å, 0.42 V/Å and 0.64 V/Å.

3. Results and discussion

3.1. Magnetron sputtering production

It is generally known that the species ejected from the target in magnetron sputtering will form films or nanometric islands on the substrate surface during the initial stage, depending on the affinity between the deposited species and the substrate. In the case of nanometric islands, only after a certain period these nanostructures coalesce and generate a continuous coating [23]. The energy of the species arriving at the substrate determines the structure, size, and distribution of the nano-islands, which depends on power density, temperature, substrate bias and mean free path in the deposition. This initial stage can be used to produce NPs, which grows primarily in a kinetically controlled process. For instance, in a previous report [5], we have demonstrated that the deposition time and power applied to a Zn target can partially control the distribution and size of Zn NPs. This study demonstrated that number of particles can be increased, such that a continuous films is formed, when the power density or the deposition

time increase. The same behaviour is observed by decreasing the working pressure during the deposition. Thus, selecting optimized deposition conditions from that report (0.2 W cm^{-2}, 240 s, 1.3 Pa), Fe was incorporated aiming to produce a galvanic couple between the Zn and Fe to better control the oxidation of the nanoparticles.

When Fe is introduced by classic magnetron sputtering, a clear alteration on the particle size and distribution is observed. Comparing Zn with ZnFe deposition, at the same power density (Fig. 2a and b respectively), a significant decrease in the deposition rate for ZnFe is observed. This phenomenon is due to the lower sputtering yield of Fe (see supplementary information Fig. S2), which promotes a decrease in the deposition rate of the system for similar discharge powers. Thus, to obtain a significant number of particles, the power of the target was systematically increased and the size and distribution of the particles were evaluated (see Fig. 2b – d).

The distribution of the NPs was notoriously modified, obtaining a remarkable homogenous size and distribution of the NPs as shown in Fig. 2c. This regular distribution of the particles shows how Fe atoms act as impurities during the Zn nucleation process, promoting sites of nucleation, and reducing the mobility of Zn, explaining the reduced size of the NPs, compared to Zn deposition. The increase in power density lead to a larger number of particles to coalesce, of the particles, reducing the number of individual particles

The Zn and Zn-Fe NPs demonstrated different growth modes. Zn forms isolated NPs, which follow the Vomer-Weber mode, while Zn-Fe grows by forming a discontinuous thin film and NPs, as depicted in Fig. 3. The decrease in the mobility of adatoms for the Zn-Fe deposition is expected due to the existence of Fe atoms on the surface, which promotes the nucleation sites, reducing their coalescence. EDX analysis of the NPs demonstrates that the film and the NPs differ in composition, showing a larger concentration of Fe in the film, as observed in Fig. 4. The elemental distribution of the as-deposited particles reveals a nanoalloy with less than 3 at. % of Fe, distributed in the entire particle (Fig. 5 e-h). Considering the phase diagram of Fe-Zn [24], for these concentrations of Fe and the distribution of Fe in the particle, the material is likely to be formed by a mixture of hexagonal Zn and a FeZn alloy (e.g. $FeZn_{13}$ or FeZn11). However, the accurate determination of the phases is not possible due to the existence of similar inter-planar distances between Zn, ZnO, $FeZn_{11}$ and $FeZn_{13}$ phases, as shown in the detailed analysis of the images presented in Fig. S3.

Additionally to the Zn and Fe signals, the EDX results revealed oxygen presence, which is dissimilar for both Zn and Zn-Fe nanoparticles (Fig. 5c and g). This oxygen presence is predictable due to the spontaneous oxidation of both metals when exposed to air. On this basis, Zn NPs showed an oxidized surface, forming core–shell structures, in agreement with previous results [5]. On the other hand, the incorporation of Fe promotes a polycrystalline growth in Zn-Fe nanostructures and prevents uniform passivation of the NPs, shown in the oxygen distribution in Fig. 5g and h.

These results show the possibility of producing both Zn NP's and Zn-Fe alloys by classic magnetron sputtering. However, to successfully build a galvanic couple between Zn and Fe, we need to avoid the formation of ZnFe alloys, forming separate phases of Zn and Fe, but in contact with each other. Thus, to attain these structures, a hybrid system between magnetrons sputtering and gas agglomeration system was utilized.

3.2. Hybrid system

In the case of the hybrid system (Zn + Fe), a gas agglomeration system coupled with a classic magnetron sputtering was used. The mode of growth in this system differs from a classic magnetron sputtering, since, on the one hand, the particles produced by magnetron sputtering growth in an atom by atom mechanism on the substrate, but on the other hand, Fe cluster are pre-formed in the agglomeration chamber at very high pressure and bombarded to the substrate through the nozzle. These clusters arrive at the substrate with specific sizes and energies depending on the agglomeration conditions. Only during the first 240 s of the process, the Zn target in the main chamber is activated (ON), making the Zn NPs grow, while the rest of the time the Fe clusters/NPs collide with the Zn particles already deposited on the substrate, promoting the redistribution of the material. The BF-TEM image in Fig. 6a shows the particles forming agglomerates, which are created after the collision of Fe NPs. A detailed analysis of these agglomerates shows the formation of polycrystalline agglomerates (cf. Fig. 6b) and an additional presence of very small clusters (~3 nm) observed on the substrate, as depicted in Fig. 6c. The surrounding area of large agglomerates shows a depletion zone of such small clusters (see Fig. S4), indicating an agglomeration mechanism caused by the collision of the Fe nanoparticles. The small clusters are identified as ZnO in the majority of the cases, and in fewer cases as Zn/ZnO particles, as observed in the digital diffraction patters in in the inset of Fig. 6c.

The analysis of the compositions of the agglomerates was performed by EDX spectrum images, demonstrating the existence of Fe NPs which are, in most of the cases, surrounded by Zn NPs, as observed in Fig. 7. The bimetallic agglomerates (for now one referred as Zn + Fe NPs), are composed of Zn and Fe NPs, exhibiting an oxidized surface. Fig. 8 shows a detailed analysis of the composition in different locations, with their respective EDX spectrum. Three zones were analyzed, a Fe rich Zone (1), a Zn rich zone (2) and the substrate (3).

3.3. Oxidation process

The three atomic arrangement produce are schematized in Fig. 9

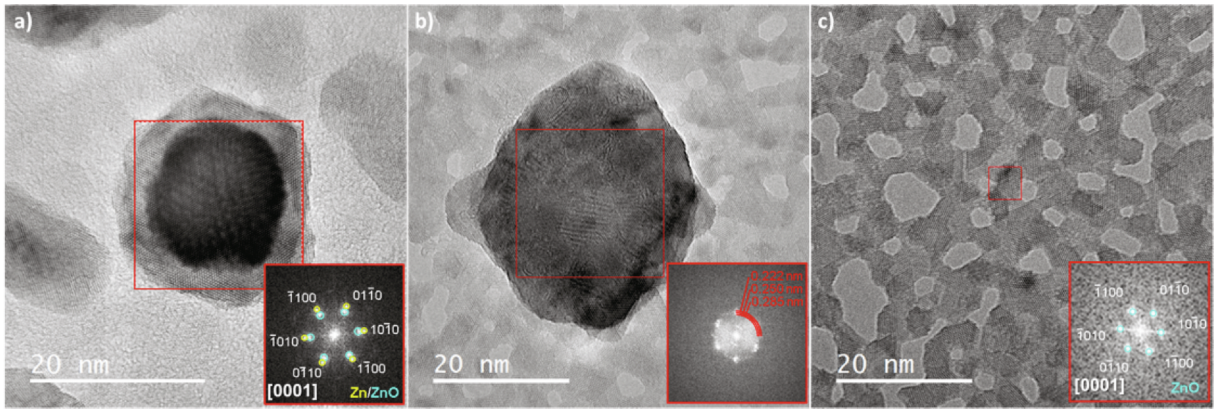

Fig. 3. Phase-contrast HR-TEM images of a) pure Zn nanostructures, b) ZnFe nanostructures, and c) ZnFe discontinuous film deposited on carbon substrates. The insets in the images represent the corresponding FFT of selected area in the red square.

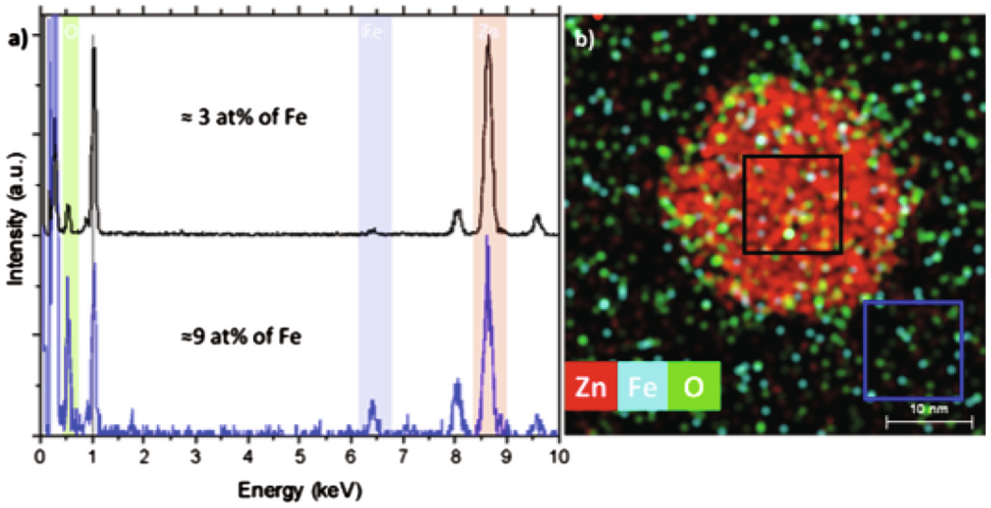

Fig. 4. a) EDX spectra of ZnFe sample acquired inside (black) and outside (blue) of the nanoparticle, as shown in b), b) EDX spectrum image acquired for ZnFe nanoparticles.

insets. These configurations were subjected to high relative environmental conditions (95–98% RH) to evaluate their oxidation mechanism. As previously reported, for high RH environments (95–98%), Zn NPs revealed that the oxidation is accompanied by a dissolution process that evolves to a ZnO layer on the carbon. This dissolution is shown in the porous structured observed in Fig. 9a, where pits are observed all over the particle, including in the centre of the particles. These particles have been meticulously characterized in a previous study and the identification of the phases can be found elsewhere [5]. Such dissolution appears to be avoided or deaccelerated by doping the Zn structures with Fe, as shown by the absence of pits on the ZnFe nanostructures (cf. Fig. 9b). This indicated more stable structures, controlling the oxidation/dissolution of the NPs, which may prevent oxygen scavenger capabilities. To interpret this behavior, it is essential to take into consideration that for high relative humidity environments, and especially for 95–98% RH, a layer of water is expected to be formed on the surface of the NPs, promoting corrosion processes. Such electrochemical processes are known to stimulate the transformation of metallic Zn to Zn^{+2} ions, in neutral/acid electrolytes [25] and, therefore, explain the dissolution of the NPs. However, at low concentration of Fe, Zn forms electrochemically stable phases such as $FeZn_{11}$ and $FeZn_{13}$, which have been demonstrated to possess a higher corrosion resistance when compared to pure Zn phases [9].

Contrary to the ZnFe alloys, the dissolution behavior is observed in the bimetallic agglomerates Zn + Fe, produced by gas agglomeration. The dissolution is evidenced by the existence of pores or pits after 1 month of exposure to the environment, as shown in Fig. 9c and Fig. 10c.

To better observe this phenomenon, HAADF-STEM images were acquired on the three systems after exposure to the 95–98% of relative humidity (Fig. 10a-c), where the pits or pores created during the dissolution are shown as dark zones inside the particle. A larger number of pits are observed for the Zn + Fe system, showing a drastic dissolution (Fig. 10c and Fig. S5), compared with the Zn and Zn-Fe systems, despite having the same exposure time to the humidity environment. EDX spectrum images also confirm the Zn depletion zones, observed for Zn

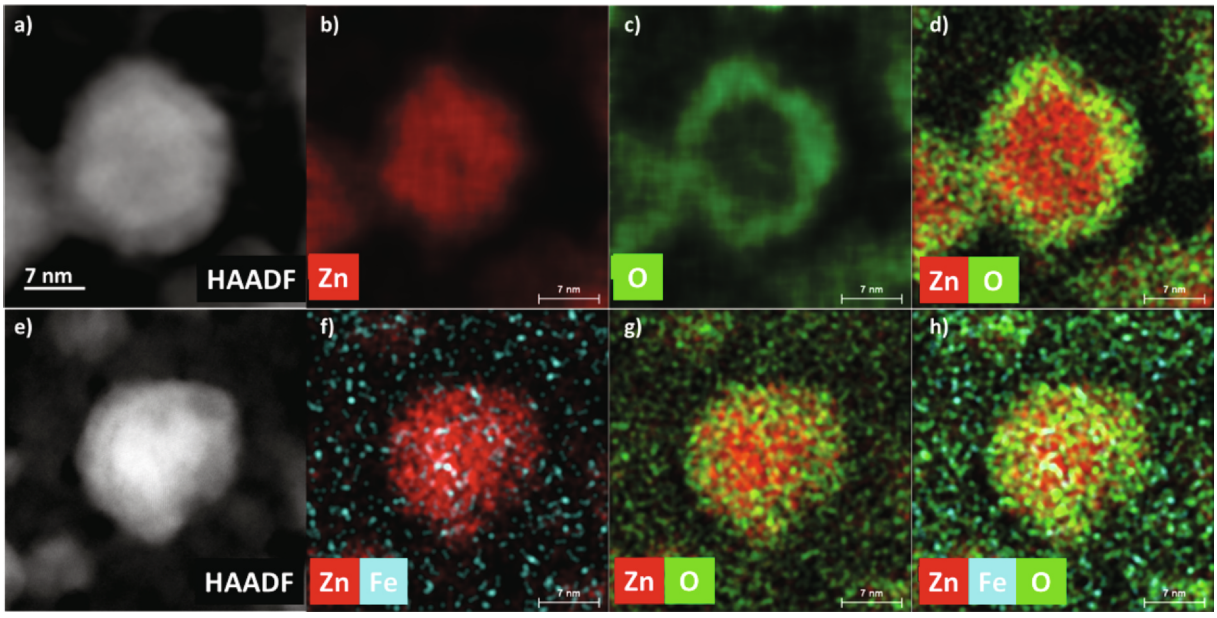

Fig. 5. (a and e) HAADF STEM images of as-deposited pure Zn and ZnFe nanoparticles, respectively, (b - d) EDX spectrum images acquired for particles shown in a) and (f - h) EDX spectrum images acquired for particles shown in e).

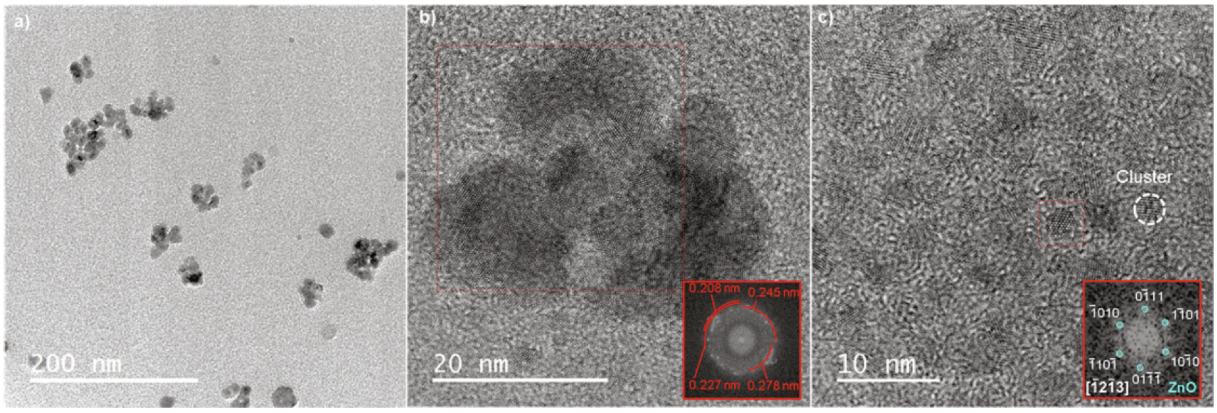

Fig. 6. a) BF-TEM images of Zn-Fe nanoparticles produced by gas agglomeration system (Zn + Fe), b) phase-contrast HR-TEM images of the agglomerates and c) phase contrast HR-TEM images of the substrate in a). The insets in the images represent the corresponding FFT of the selected area in the red square.

and Zn + Fe nanostructures, while Zn-Fe NPs exhibit a passivated surface, forming core–shell structures. Remarkably, the dissolution of the Zn is more predominantly observed for the Zn + Fe agglomerates, when compared to the other two systems, confirming the galvanic activation process.

The acceleration in the oxidation rate for Zn + Fe nanostructures is explained by the dissimilar corrosion potential of zinc and iron. In pure water, these two metals show a difference of the redox potential of approximately 320 mV [26], creating a galvanic couple, where the Zn behaves as the anode and the Fe as the cathode in the reaction. This process is potentiated by the carbon substrate, which acts as a more noble material. On the other hand, we attribute the lack of dissolution of Zn-Fe structures to the formation of FeZn alloys, which present a higher corrosion resistance when compared to a pure Zn phase, as previously mentioned.

3.4. ReaxFF molecular dynamic simulations

Molecular dynamic simulations were carried out to evaluate the effect of the galvanic couple on the water dissociation and Zn/ZnO dissolution on the surface of Zn and ZnO. First, a (0 0 0 1) ZnO surface is exposed to water and the evolution of the oxygen, Zn atoms and water molecules are monitored. In this simulation, Fe was not directly included due to the complexity in the interatomic potential required to simulate Zn and Fe phases. However, as demonstrated by the experimental results, the effect of Fe is mainly to create a galvanic pair that promotes the existence of an electric field in humid environments.

For Zn, the initial oxide is formed in contact with an oxygen atmosphere, due to the adsorption of oxygen on the Zn surface, forming an oxide layer that stabilize around 2.7 nm, as discussed elsewhere [5]. By introducing humidity in the environment, ZnO becomes unstable against the formation of zinc vacancies, favoring the dissolution of oxide [23].

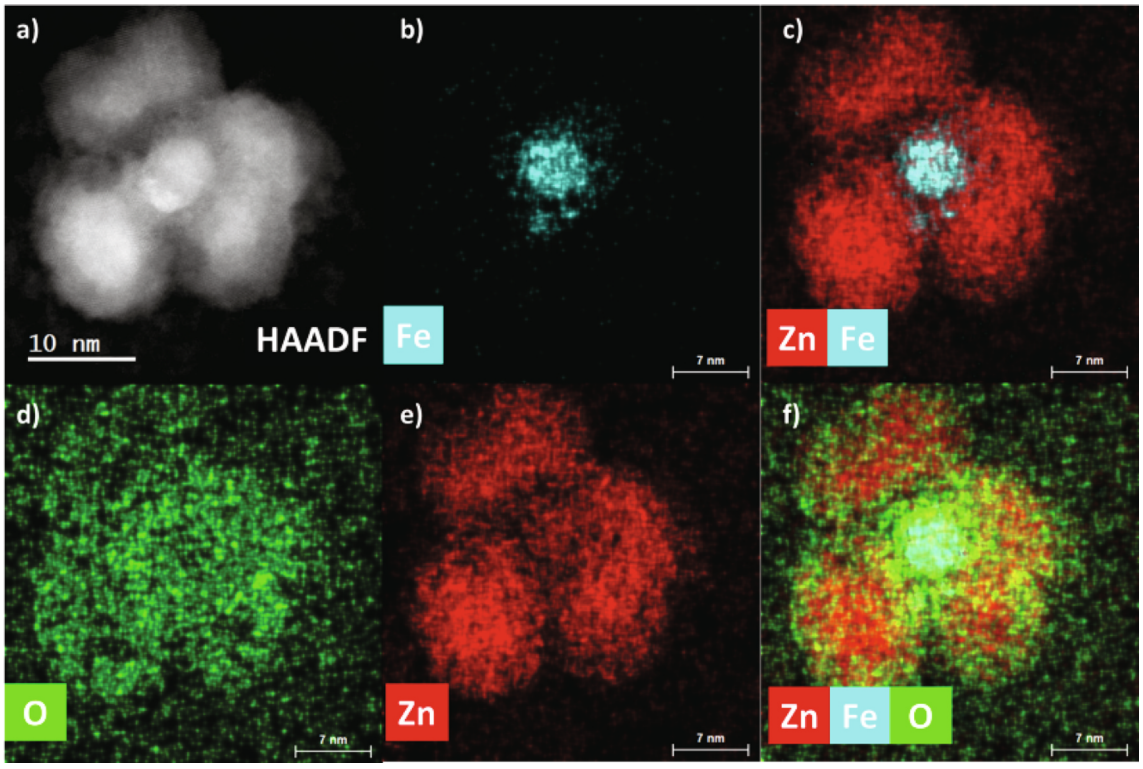

Fig. 7. (a) HAADF STEM images of as-deposited Zn + Fe nanoparticles, (b - f) EDX spectrum images acquired for the particle.

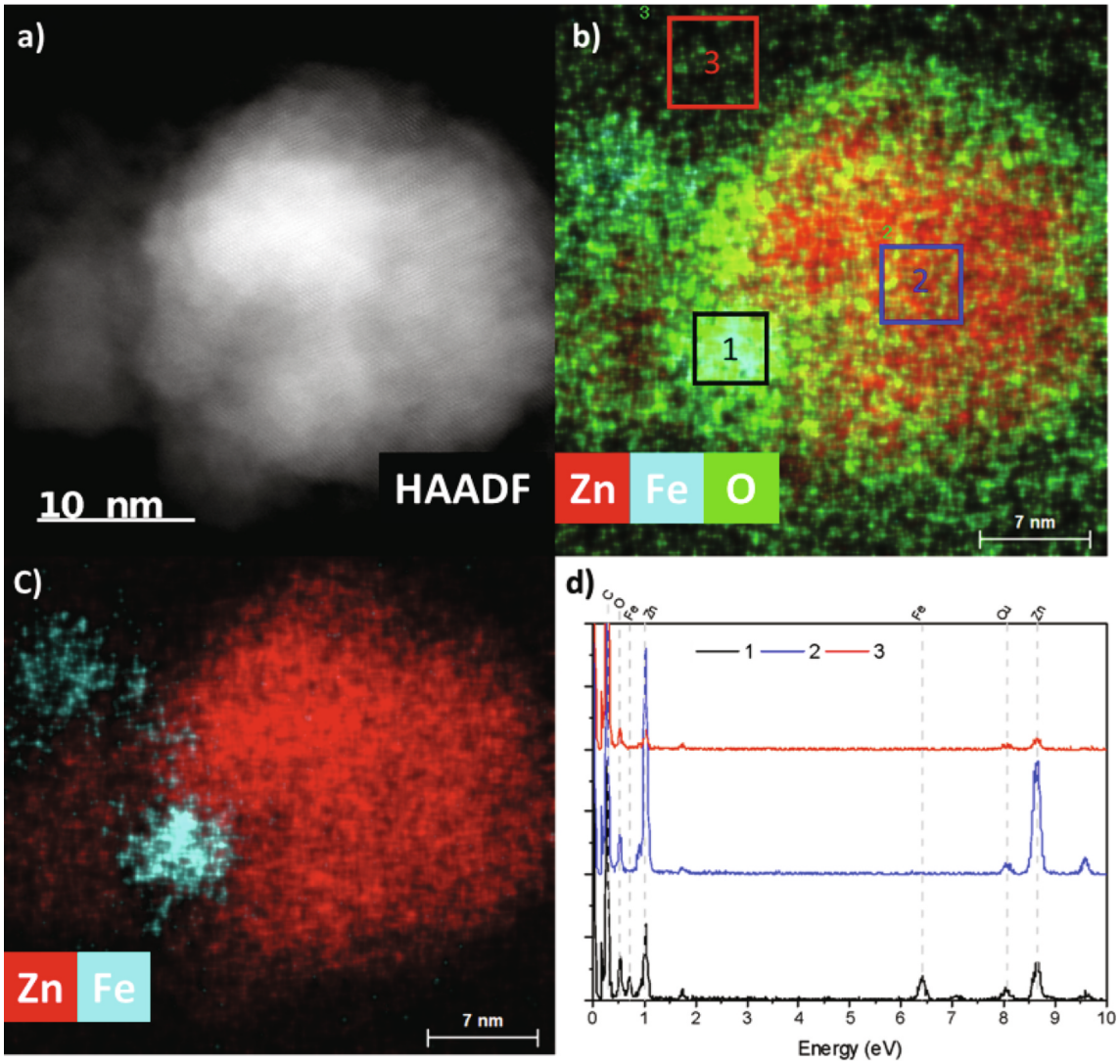

Fig. 8. (a) HAADF STEM image of as-deposited Zn + Fe nanoparticles, (b - c) EDX spectrum images acquired for the particle shown in a), and (d) EDX spectra in different zones highlighted in figure b).

Fig. 11a and b show the initial and final state of the model for 0 electric field. For this case, the formation of a Zn-OH layer is evidenced, creating a small separation between the water and the ZnO of about 1.4A, as shown in detail in Fig. 11d. The formation of the hydroxide is well-known and has been reported to be one of the steps on the oxidation of the Zn. However, no significant dissolution of zinc is observed during the 200 ps of simulation. When a constant electric field is applied, to mimic the galvanic couple effect, the Zn atoms on the surface start to move to the interior of the double layer, evidencing the acceleration of the corrosion process, as shown in Fig. 12. Additionally, dissolution of Zn become evident for electric fields larger than 0.32 V/Å and a significant amount of Zn moves to the liquid phase for 0.42 V/Å.

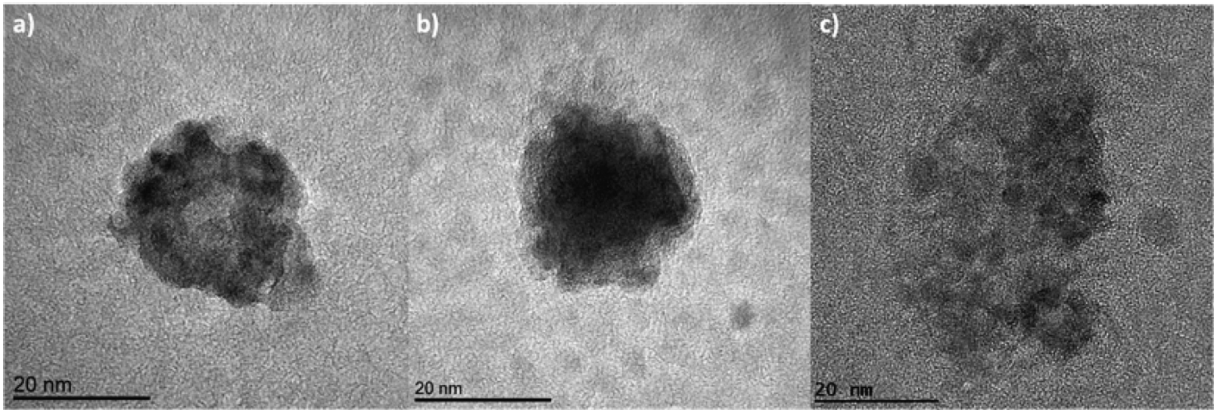

Fig. 9. Phase-contrast images of the nanostructures after 1 month in a high humidity environment (95–98% RH) for a) Zn, b) ZnFe, c) Zn + Fe.

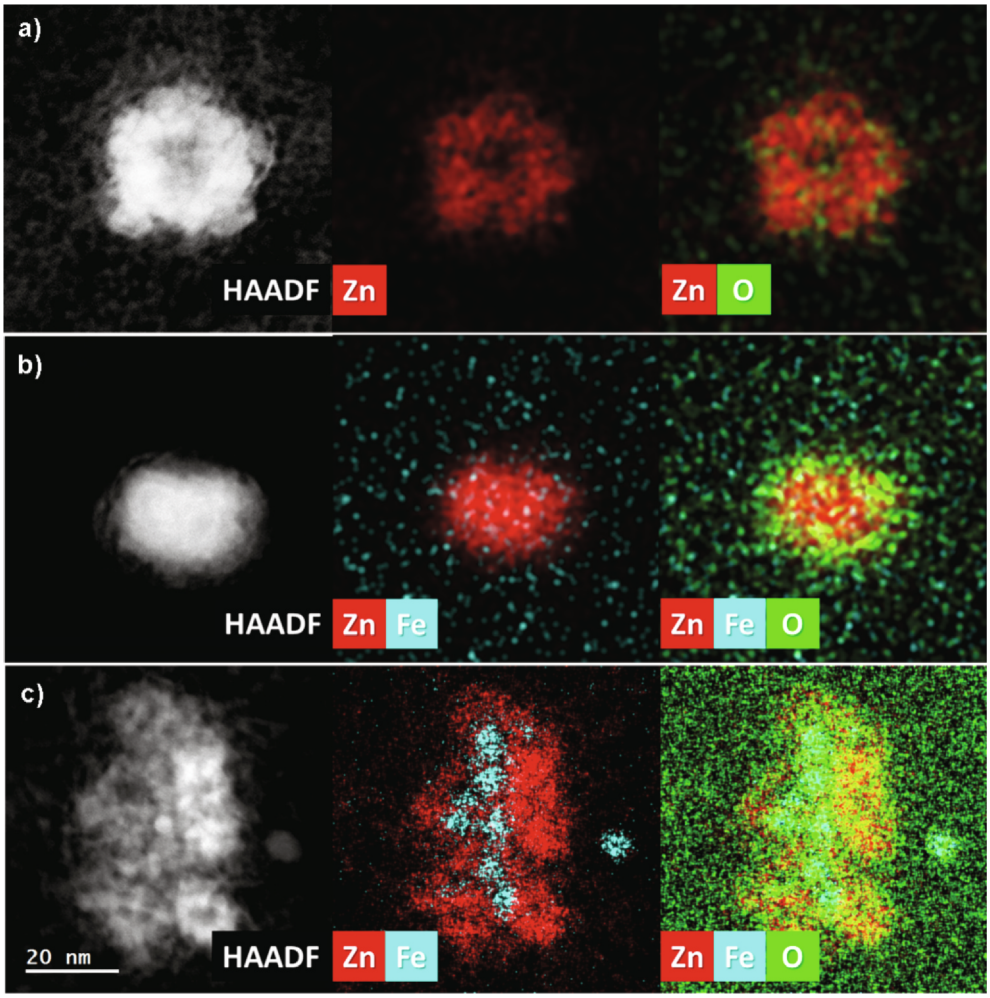

Fig. 10. (a - c) HAADF STEM images of Zn, ZnFe, Zn + Fe nanostructures, after 1 month exposed to 95–98% RH environment, with their corresponding EDX spectrum images.

These results demonstrate the acceleration of the dissolution when a galvanic couple is introduced, caused by the increase in the driving force for the ions to diffuse. For larger electric fields (0.64 V/Å) the structure is disrupted and the surface collapses, which may be interpreted as a breakdown potential.

The evolution of water molecules as a function of time was also analyzed and is depicted in Fig. 12g. For all the electric fields, the number of molecules significantly decreased during the first 20 ps, which is attributed to two phenomena, (i) water adsorption on the surface and (ii) water dissociation forming the zinc hydroxide phases. However, for each applied electric field the water molecules stabilize at different values. Such plateau is not completely attained for 0.62 V/Å, due to the continuous dissolution of Zn. Fig. 12h, show the number of water molecules at the end of the simulation time (0.2 ns). The number of water molecules increases as the electric field increases up to 0.2 V/Å, which is attributed to the desorption process caused by the polarization of the surface. Nonetheless, as the electric field increases, the dissolution of the metal promotes more water to be in contact with Zn and thus, stimulating the water dissociation.

4. Conclusions

In summary, we study Zn-Fe NPs synthesized by two methods, demonstrating a simple production of bimetallic systems using a hybrid magnetron sputtering and gas agglomeration chamber. The different atomic arrangements of the Zn and Fe allow the control of the moisture-activated oxidation mechanism, accelerating the oxidation process for NPs with separated Zn and Fe phases while decelerating the process for ZnFe alloys. Sputtering Zn from a classic magnetron sputtering and Fe from a cluster gun produces an atomic configuration that promotes a galvanic couple formation, which in the presence of high humidity environment create a difference of potential between the two phases and thus, accelerate the oxidation process. Co-sputtering Zn and Fe from the same target, on the other hand, promotes the formation of ZnFe alloys, decreasing the oxidation rates in the systems.

CRediT authorship contribution statement

A. Castro: Investigation. **I. Carvalho:** Investigation. **L. Marques:** Supervision. **P.J. Ferreira:** Supervision. **A. Cavaleiro:** Supervision. **S. Carvalho:** Supervision, Funding acquisition. **S. Calderon:** Conceptualization, Methodology, Writing - review & editing, Funding acquisition.

Declaration of Competing Interest

The authors declare that they have no known competing financial interests or personal relationships that could have appeared to influence the work reported in this paper.

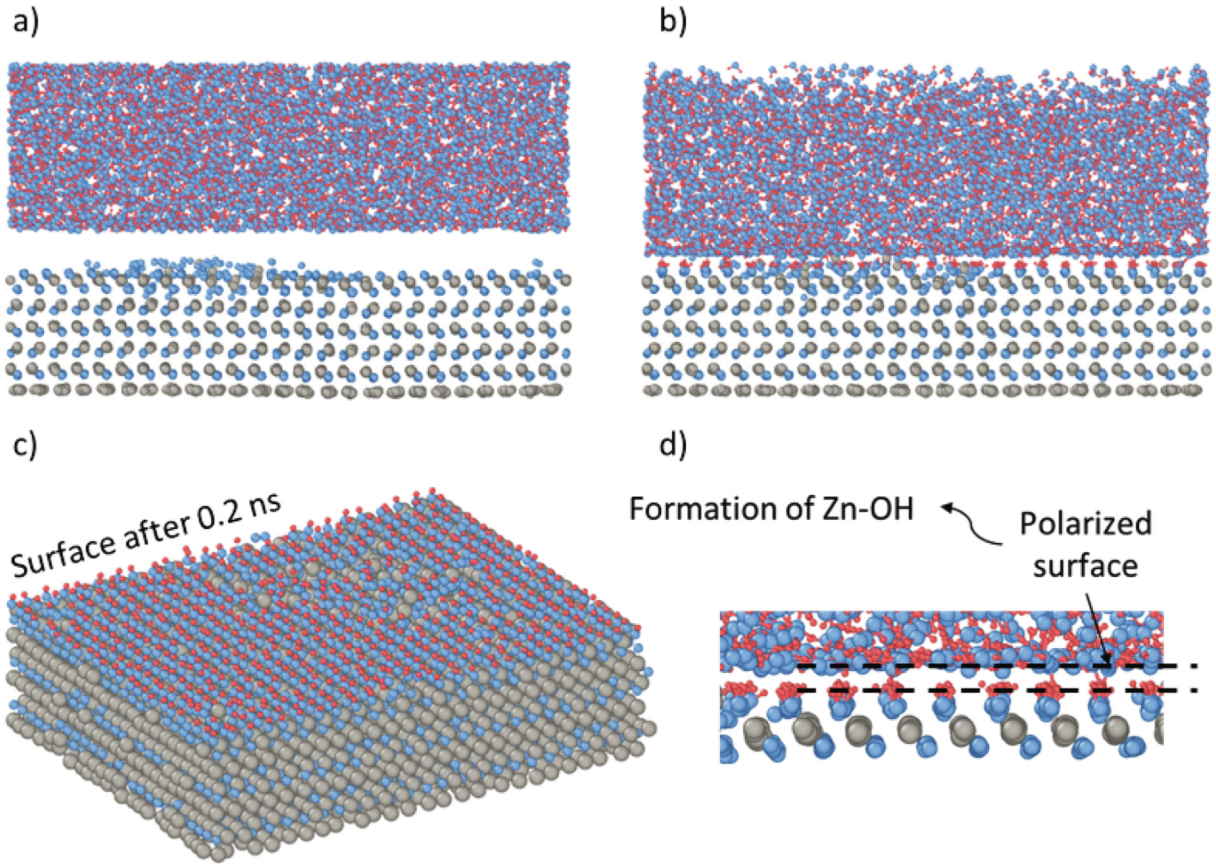

Fig. 11. Side view ZnO- H_2O model (a) after relaxation time, (b) after 200 ps, (c) the dissociation of water on the ZnO surface and (d) detail view of the surface after 0.2 nm. Red, blue, and grey spheres represent H, O, and Zn atoms, respectively.

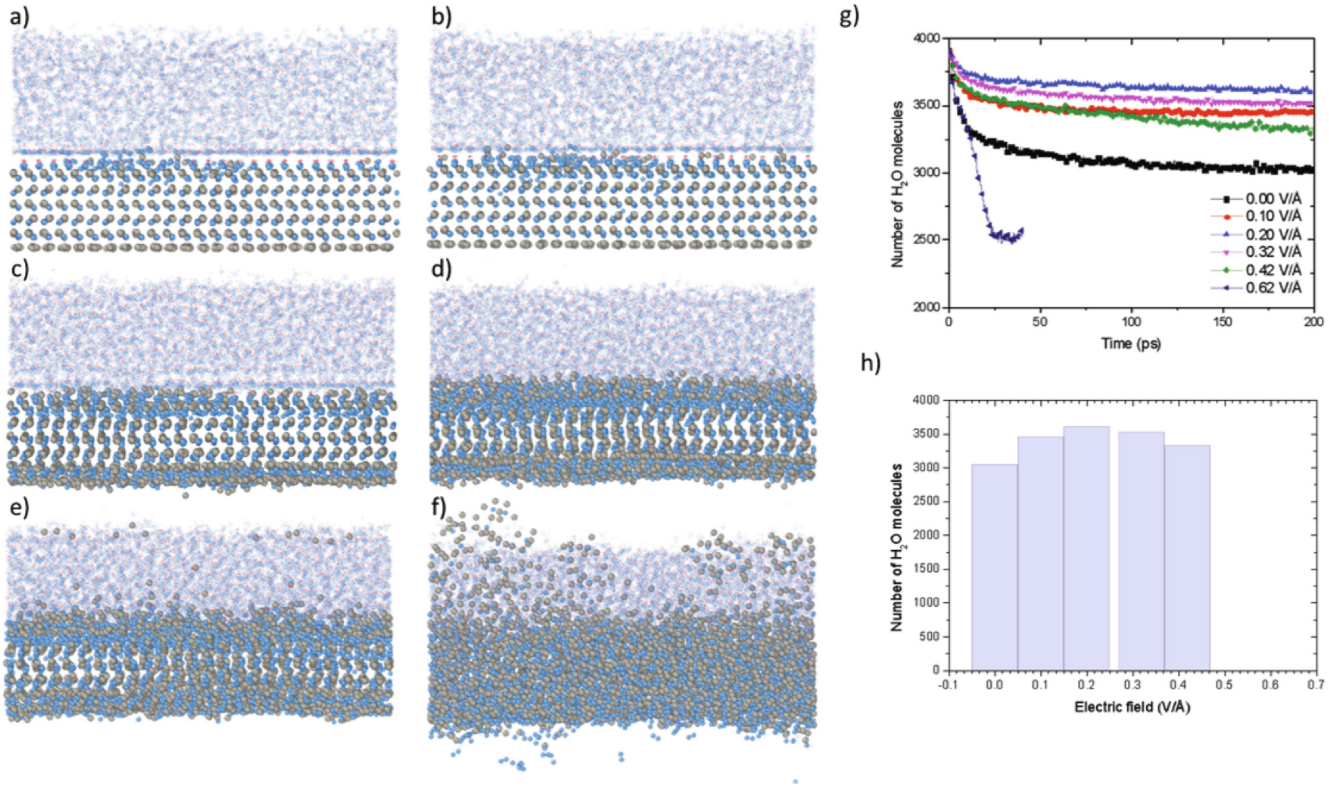

Fig. 12. Side view ZnO-H_2O model after 200 ps under an electric field (a) 0 V/Å, (b) 0.10 V/Å, (c) 0.20 V/Å, (d) 0.32 V/Å, (e) 0.42 V/Å, (f) 0.64 V/Å, (g) evolution of H_2O molecules as a function of time and (h) number of H_2O molecules after 200 ps for each potential.

Acknowledgements

This research is sponsored by FEDER funds through the program COMPETE – Programa Operacional Factores de Competitividade and by the Portuguese Foundation for Science and Technology (FCT) in the framework of the Strategic Funding UID/FIS/04650/2019, and UID/EMS/00285/2013 and in the framework of ERA-SIINN/0004/2013, PTDC/CTM-NAN/4242/2014 and PTDC/NAN-MAT/30789/2017 projects, and through IDMEC, under LAETA, project UIDB/50022/2020. This research was supported by Norte Regional Operational Program 2014-2020 (Norte2020) through the European Regional Development Fund (ERDF) Nanotechnology based functional solutions (NORTE-01-0145-FEDER-000019) and through European Social Fund (FSE), under the National Doctoral Program in "Surfaces Engineering and Protection", NORTE-08-5369-FSE-000047. The authors would like to acknowledge that this project received funding from the EU Framework Programme for Research and Innovation H2020, scheme COFUND – Co-funding of Regional, National and International Programmes, under Grant Agreement 713640. The authors also thank the financial support by Portuguese Foundation for Science and Technology (FCT) in the framework of the HEALTHYDENT (co-financed via FEDER (PT2020) POCI-01-0145-FEDER-030708 and FCT (PIDDAC)), in the framework of the ATRITO-0 (co-financed via FEDER (PT2020) POCI-01-0145-FEDER-030446 and FCT (PIDDAC)) and in the framework of the project NANOXYPACK co-financed via FEDER (PT2020) POCI-01-0145-FEDER-030789.

Appendix A. Supplementary data

Supplementary data to this article can be found online at https://doi.org/10.1016/j.apsusc.2020.147896.

References

[1] H. Zeng, W. Cai, Y. Li, J. Hu, P. Liu, Composition/Structural Evolution and Optical Properties of ZnO/Zn Nanoparticles by Laser Ablation in Liquid Media, J. Phys. Chem. B 109 (39) (2005) 18260–18266.
[2] C. Rao, P. Thomas, K.G. Nanocrystals, Synthesis Properties Appl. (2007).
[3] D.V. Talapin, E.V. Shevchenko, Introduction: Nanoparticle Chemistry, Chem. Rev. 116 (18) (2016) 10343–10345.
[4] F.J. Heiligtag, M. Niederberger, The Fascinating World of Nanoparticle Research, Mater. Today 16 (7–8) (2013) 262–271.
[5] S.V. Calderon, B. Gomes, P.J. Ferreira, S. Carvalho, Zinc Nanostructures for Oxygen Scavenging, Nanoscale 9 (2017) 16.
[6] H.H. Haberland, Some Basics, and an Outlook, Gas-Phase Synth Nanoparticles (2017) 1–21.
[7] J. Vernieres, S. Steinhauer, J. Zhao, A. Chapelle, P. Menini, N. Dufour, R.E. Diaz, K. Nordlund, F. Djurabekova, P. Grammatikopoulos, M. Sowwan, Gas Phase Synthesis of Multifunctional Fe-Based Nanocubes, Adv. Funct. Mater. 27 (11) (2017).
[8] N.K. Manninen, N.M. Figueiredo, S. Carvalho, A. Cavaleiro, Production and Characterization of Ag Nanoclusters Produced by Plasma Gas Condensation, Plasma Process. Polym. 11 (7) (2014) 629–638.
[9] A.P. Yadav, Effect of Fe – Zn Alloy Layer on the Corrosion Resistance of Galvanized Steel in Chloride Containing, Environments. 49 (2007) 3716–3731.
[10] J. Zhao, E. Baibuz, J. Vernieres, P. Grammatikopoulos, V. Jansson, M. Nagel, S. Steinhauer, M. Sowwan, A. Kuronen, K. Nordlund, F. Djurabekova, Formation Mechanism of Fe Nanocubes by Magnetron Sputtering Inert Gas Condensation, ACS Nano 10 (4) (2016) 4684–4694.
[11] H.T. Nasrabadi, E. Abbasi, S. Davaran, M. Kouhi, A. Akbarzadeh, Bimetallic Nanoparticles: Preparation, Properties, and Biomedical Applications, Artif. Cells, Nanomed., Biotechnol. 44 (1) (2016) 376–380.
[12] J. Schindelin, I. Arganda-Carreras, E. Frise, V. Kaynig, M. Longair, T. Pietzsch, S. Preibisch, C. Rueden, S. Saalfeld, B. Schmid, J.Y. Tinevez, D.J. White, V. Hartenstein, K. Eliceiri, P. Tomancak, A. Cardona, Fiji: An Open-Source Platform for Biological-Image Analysis, Nat. Methods 9 (7) (2012) 676–682.
[13] D.J. Groom, K. Yu, S. Rasouli, J. Polarinakis, A.C. Bovik, P.J. Ferreira, Automatic segmentation of inorganic nanoparticles in BF TEM micrographs, Ultramicroscopy 194 (2018).
[14] A.C.T. van Duin, S. Dasgupta, F. Lorant, W.A. Goddard, ReaxFF: A Reactive Force Field for Hydrocarbons, J. Phys. Chem. A 105 (41) (2001) 9396–9409.
[15] D. Raymand, A.C.T. van Duin, D. Spångberg, W.A. Goddard, K. Hermansson, Water Adsorption on Stepped ZnO Surfaces from MD Simulation, Surf. Sci. 604 (9–10) (2010) 741–752.
[16] A.K. Rappe, W.A. Goddard, Charge Equilibration for Molecular Dynamics Simulations, J. Phys. Chem. 95 (8) (1991) 3358–3363.
[17] A. Nakano, Parallel Multilevel Preconditioned Conjugate-Gradient Approach to Variable-Charge Molecular Dynamics, Comput. Phys. Commun. 104 (1–3) (1997) 59–69.
[18] S. Plimpton, Fast Parallel Algorithms for Short-Range Molecular Dynamics, J. Comput. Phys. 117 (1) (1995) 1–19.
[19] H.M. Aktulga, J.C. Fogarty, S.A. Pandit, A.Y. Grama, Parallel Reactive Molecular Dynamics: Numerical Methods and Algorithmic Techniques, Parallel Comput. 38 (4–5) (2012) 245–259.
[20] S. Nosé, A Unified Formulation of the Constant Temperature Molecular Dynamics Methods, J. Chem. Phys. 81 (1) (1984) 511–519.
[21] W.G. Hoover, Canonical Dynamics: Equilibrium Phase-Space Distributions, Phys. Rev. A 31 (3) (1985) 1695–1697.
[22] W.C. Swope, H.C. Andersen, P.H. Berens, K.R. Wilson, A Computer Simulation Method for the Calculation of Equilibrium Constants for the Formation of Physical Clusters of Molecules: Application to Small Water Clusters, J. Chem. Phys. 76 (1) (1982) 637–649.
[23] H. Search, C. Journals, A. Contact, M. Iopscience, I.P. Address, Nucleation and Growth of, Thin Films. (1984) 399.
[24] R.H. Davies, A.T. Dinsdale, J.A. Gisby, J.A.J. Robinson, S.M. Martin, MTDATA - Thermodynamic and Phase Equilibrium Software from the National Physical Laboratory, Calphad Comput. Coupling Phase Diagrams Thermochem. 26 (2) (2002) 229–271.
[25] B. Beverskog, I. Puigdomenech, Revised Pourbaix Diagrams for Zinc at 25–300 °C, Corros. Sci. 39 (1) (1997) 107–114.
[26] Baker, D. General Chemistry, 5th Ed. (Ebbing, Darrell D.). J. Chem. Educ. 1997, 74 (9), 1049.